was later resected and over both whole lungs by a chest radiologist with 5 years of experience. All ROI measurements were performed on the same PC with commercially available software (iNRT, Nihon Medi-Physics, Nisihinomiya, Japan). Each prediction of postoperative lung function (FEV_1) assessed with SPECT was estimated with the following formula [24]:

$$\text{Postoperative } FEV_1 \text{ from perfusion SPECT} = \text{Postoperative } FEV_1 \times \left(1 - \frac{\text{Summed radioactivity within ROIs placed over resected lobe}}{\text{Total lung volume activity}}\right)$$

Physiologic Index and Outcome Measures

Pulmonary function testing was performed according to American Thoracic Society standards with an automatic spirometer (System 9, Minato Ikagaku). All subjects underwent preoperative and postoperative pulmonary function testing. All preoperative pulmonary function spirometric tests were performed within 2 weeks (mean, 6.4 days) before MRI. All postoperative pulmonary function spirometric tests were performed within 24–48 weeks (mean, 32 weeks) after surgery. Pulmonary function testing was performed according to American Thoracic Society standards [25, 26].

Statistical Analysis

To determine the utility of dynamic perfusion MRI in prediction of postoperative lung function, the correlation and limits of agreement between each version of predicted postoperative FEV_1 and the actual postoperative FEV_1 were statistically evaluated. Limits of agreement between actual and predicted postoperative FEV_1 were analyzed by means of Bland-Altman analysis. Statistical significance was $p < 0.05$ for all analyses. The basic theory and application of the limits of agreement have been documented in the literature [27].

Results

A representative case is shown in Figure 1. Correlation between the predicted postoperative FEV_1 value for each method of measurement and the corresponding actual postoperative FEV_1 (FEV_1 values expressed as percentage of predicted value) is shown in Figure 2. The postoperative FEV_1 values predicted from perfusion MRI ($r = 0.87$, $r^2 = 0.76$, $p < 0.0001$) and quantitative CT assessment ($r = 0.88$, $r^2 = 0.77$, $p < 0.0001$) had better correlation with actual postoperative FEV_1 than did postoperative FEV_1 predicted from qualitative CT assessment ($r = 0.83$, $r^2 = 0.69$, $p < 0.0001$) and perfusion SPECT ($r = 0.83$, $r^2 = 0.69$, $p < 0.0001$). Despite the differences in results between methods, all four versions of predicted postoperative FEV_1 correlated well with actual postoperative FEV_1.

The mean of difference and the limits of agreement between actual postoperative FEV_1 and each predicted postoperative FEV_1 are shown in Figure 3. For postoperative FEV_1 predicted from perfusion MRI, the mean and standard error were 5.3% ± 0.5% and the limits of agreement were between –6.5% and 17.1%. For postoperative FEV_1 predicted from quantitative CT, the corresponding values were 5.0% ± 0.5%, and between –6.6% and 16.6%. For postoperative FEV_1 predicted from qualitative CT, they were 6.8% ± 0.6%, and between –7.6% and 21.2%; and for postoperative FEV_1 predicted from perfusion SPECT, 5.1% ± 0.6%, and between –8.9% and 19.1%.

Discussion

Our results show the utility of dynamic perfusion MRI in prediction of postoperative lung function after pulmonary resection in a large prospective cohort of patients with lung cancer. With this technique, regional pulmonary function can be assessed on the basis of pulmonary perfusion without radiation exposure [11, 14–19]. In addition, to the best of our knowledge, this study is the first in which the capability of dynamic perfusion MRI is compared directly with that of quantitative and qualitative CT and perfusion SPECT.

The comparison of actual and predicted postoperative FEV_1 values showed that the correlation and limits of agreement between postoperative FEV_1 predicted from perfusion MRI and the actual value were superior to those of postoperative FEV_1 predicted from qualitative CT and perfusion SPECT and similar to those of postoperative FEV_1 predicted from quantitative CT. Because the limits of agreement of dynamic contrast-enhanced perfusion MRI are considered small enough for clinical purposes, dynamic perfusion MRI can be substituted for perfusion SPECT and qualitative CT in prediction of postoperative lung function and can be considered as at least as useful as quantitative CT.

For prediction of postoperative lung function with dynamic perfusion MRI, regional and total functional lung volumes were assessed on the basis of regional perfusion assessed in a manner similar to the procedure for perfusion SPECT. Our results suggest that dynamic perfusion MRI is better than is perfusion SPECT for assessment of regional functional lung volume. This finding is based mainly on the following characteristics of dynamic perfusion MRI: higher spatial resolution for assessment of resected segments and lobes not including large vessels; less gravitational influence on regional perfusion parameters, because of the small molecular size and weight of gadopentetate dimeglumine; and greater accuracy of calculation of regional and total lung volumes, because of the use of regional pulmonary perfusion data obtained from the signal intensity–time course curve. Previous studies [11, 17] have shown that regional perfusion parameters semiquantitatively or quantitatively assessed with dynamic perfusion MRI had good or excellent correlation with those assessed with perfusion scintigraphy. It has been suggested [11, 17] that dynamic perfusion MRI has similar or slightly better utility than perfusion scintigraphy for prediction of postoperative lung function. Our results are compatible with the previous results, even when perfusion SPECT is substituted for perfusion scintigraphy. Perfusion scintigraphy with or without SPECT has been proposed as the reference standard for estimating postoperative lung function after lung resection in the treatment of lung cancer patients. However, perfusion scintigraphy may well be replaced by dynamic perfusion MRI in the near future.

For comparison with quantitative CT assessment, predicted postoperative FEV_1 was calculated from regional and total functional lung volumes. The latter was determined by subtracting from the entire lung volume the nonfunctional lung volume resulting from pulmonary emphysema, tumor, atelectasis, and fibrosis identified by segmentation based on attenuation in the lung. Our results and those reported by others [9, 10, 20] indicate that this method can be considered the most accurate for prediction of postoperative lung function. The aforementioned pathologic conditions are assessed according to the underlying physiopathologic features by use of semiquantitatively or quantitatively assessed regional pulmonary perfusion parameters on dynamic perfusion MRI. Therefore, our results suggest that dynamic perfusion MRI is at least as valuable as quantitative CT for prediction of postoperative lung function.

In contrast to quantitative CT assessment, qualitative assessment of CT scans on the basis

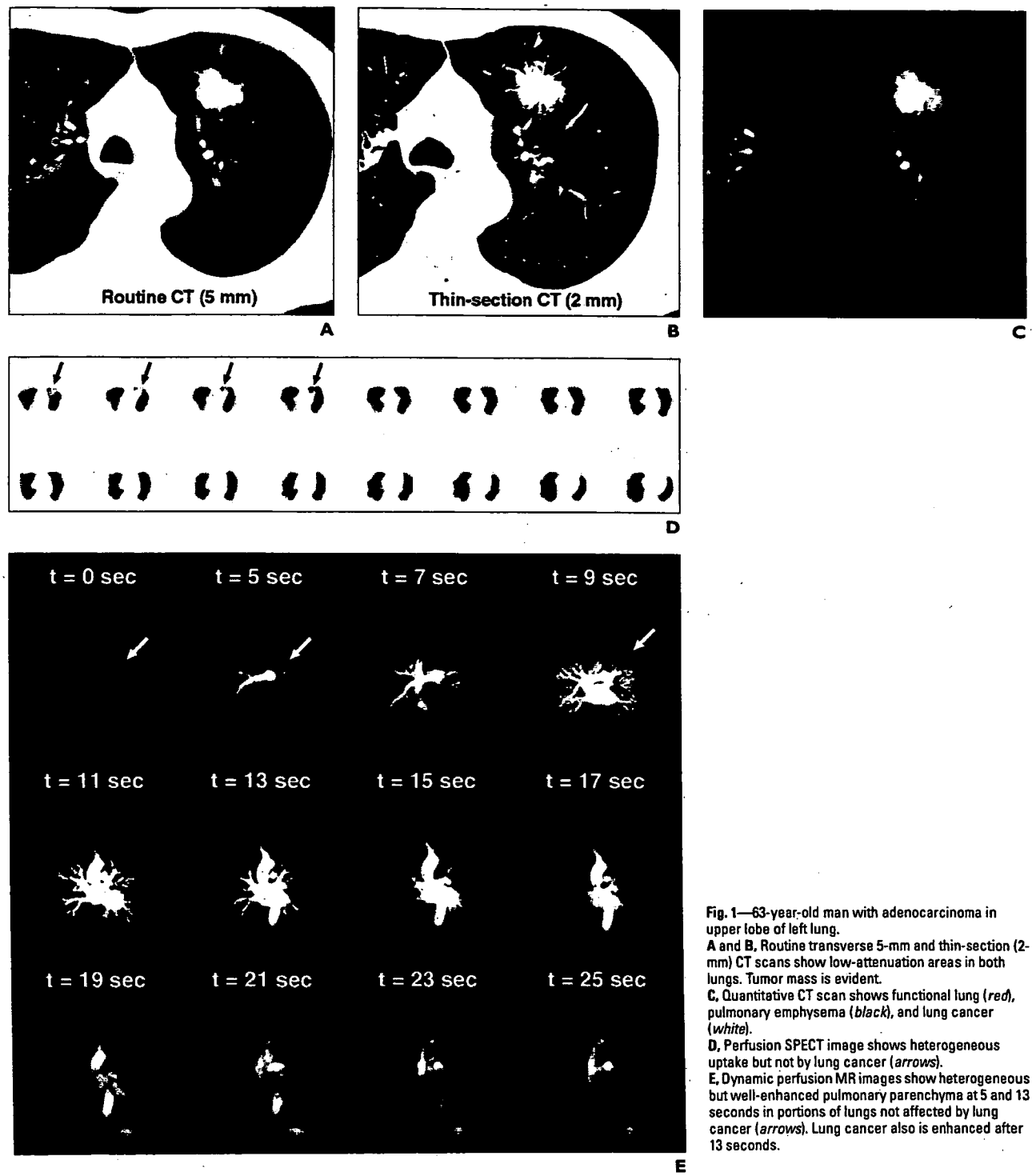

Fig. 1—63-year-old man with adenocarcinoma in upper lobe of left lung.
A and **B**, Routine transverse 5-mm and thin-section (2-mm) CT scans show low-attenuation areas in both lungs. Tumor mass is evident.
C, Quantitative CT scan shows functional lung (*red*), pulmonary emphysema (*black*), and lung cancer (*white*).
D, Perfusion SPECT image shows heterogeneous uptake but not by lung cancer (*arrows*).
E, Dynamic perfusion MR images show heterogeneous but well-enhanced pulmonary parenchyma at 5 and 13 seconds in portions of lungs not affected by lung cancer (*arrows*). Lung cancer also is enhanced after 13 seconds.

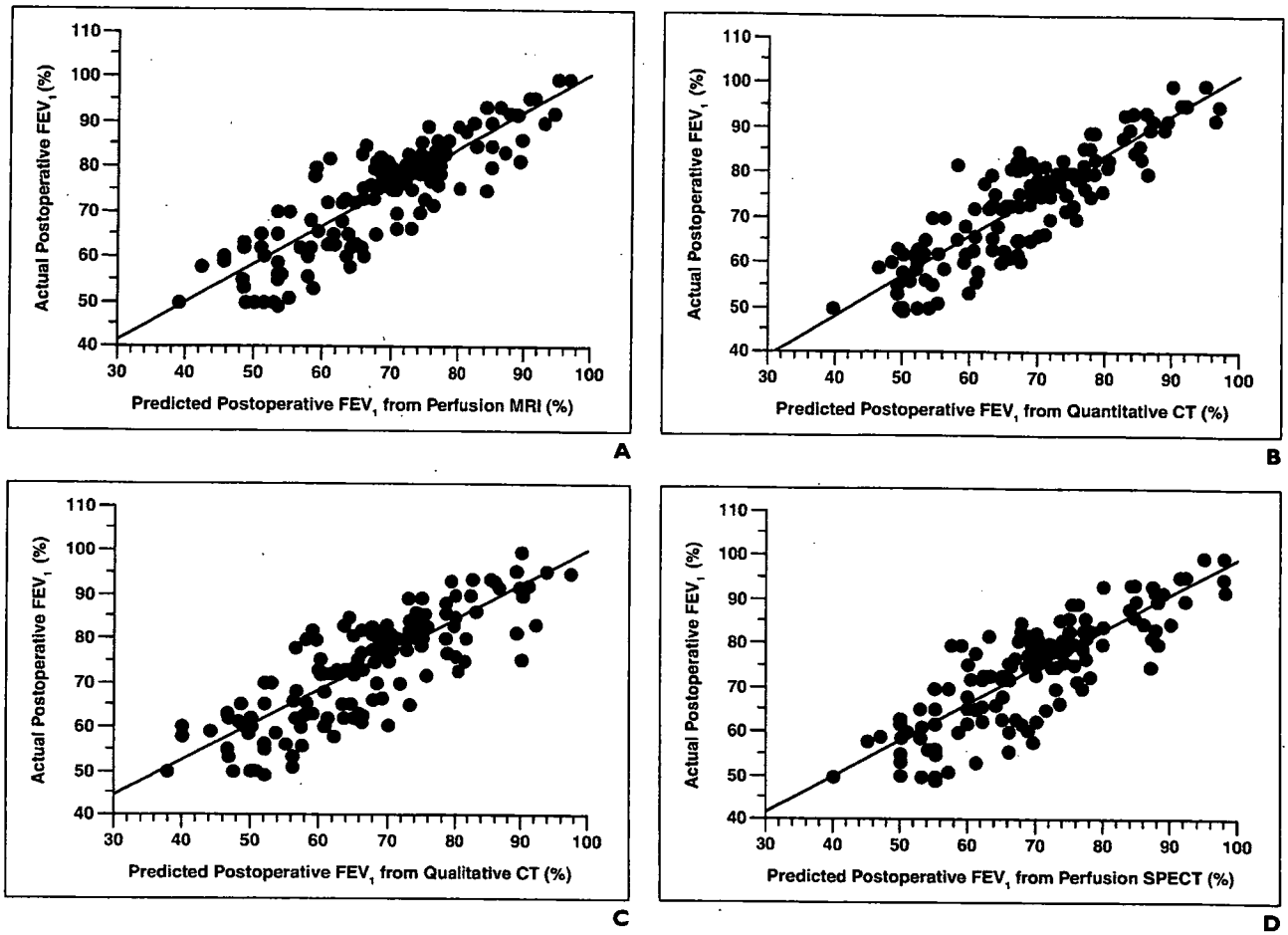

Fig. 2—Correlation between each version of predicted postoperative forced expiratory volume in first second of expiration (FEV_1), expressed as percentage of predicted value, and actual postoperative FEV_1.
A, Graph shows postoperative FEV_1 predicted from perfusion MRI correlates well ($r = 0.87$, $p < 0.0001$) with actual postoperative FEV_1.
B, Graph shows postoperative FEV_1 predicted from quantitative assessment of CT scans correlates well ($r = 0.88$, $p < 0.0001$) with actual postoperative FEV_1.
C, Graph shows postoperative FEV_1 predicted from qualitative assessment of CT scans correlates well ($r = 0.83$, $p < 0.0001$) with actual postoperative FEV_1.
D, Graph shows postoperative FEV_1 predicted from perfusion SPECT correlates well ($r = 0.83$, $p < 0.0001$) with actual postoperative FEV_1.

of number of bronchopulmonary segments is performed with a simple calculation method, and IV administration of contrast medium is not necessary.Many surgical institutions claim that this simple calculation provides a satisfactory estimate of operative risk. This claim is true for surgical candidates who are at low risk and have good results of preoperative pulmonary function tests, but we found that the correlation coefficient was lower and limits of agreement greater for qualitative CT assessment than for the other methods of prediction. These findings suggest that the greater overestimation and underestimation of postoperative FEV_1 with this simple calculation than with other methods may be due to omission of evaluation of associated pulmonary emphysema, functional loss due to obstructive atelectasis and presence of nonfunctional lung area surrounding lung cancer, ventilation–perfusion mismatch due to invasion of the pulmonary vasculature by central lung cancer, the presence of hilar lymph node metastasis, and differences in size among various segments. When pulmonary resection is being considered in the treatment of high-risk surgical candidates, dynamic perfusion MRI or quantitative CT even with perfusion SPECT may be helpful for more accurate prediction of postoperative FEV_1 in patients with non–small cell lung cancer.

There were limitations to this study. First, although all dynamic perfusion MRI examinations were successfully completed without adverse effects and regional perfusion was completely calculated from signal intensity–time course curves, 12 lung cancer patients with severe chronic obstructive pulmonary disease needed to breathe shallowly for data acquisition, resulting in slight deterioration of image quality. In lung cancer patients with poor pulmonary function, poor breath-hold capability can result in underestimation of regional perfusion and regional pulmonary function. However, because dynamic perfusion MRI is a new technique for estimation of postoperative lung function, advances leading to faster imaging time may make this technique more practical than earlier techniques.

A second limitation was that measurement of regional pulmonary perfusion parameters with the indicator dilution method is a semi-

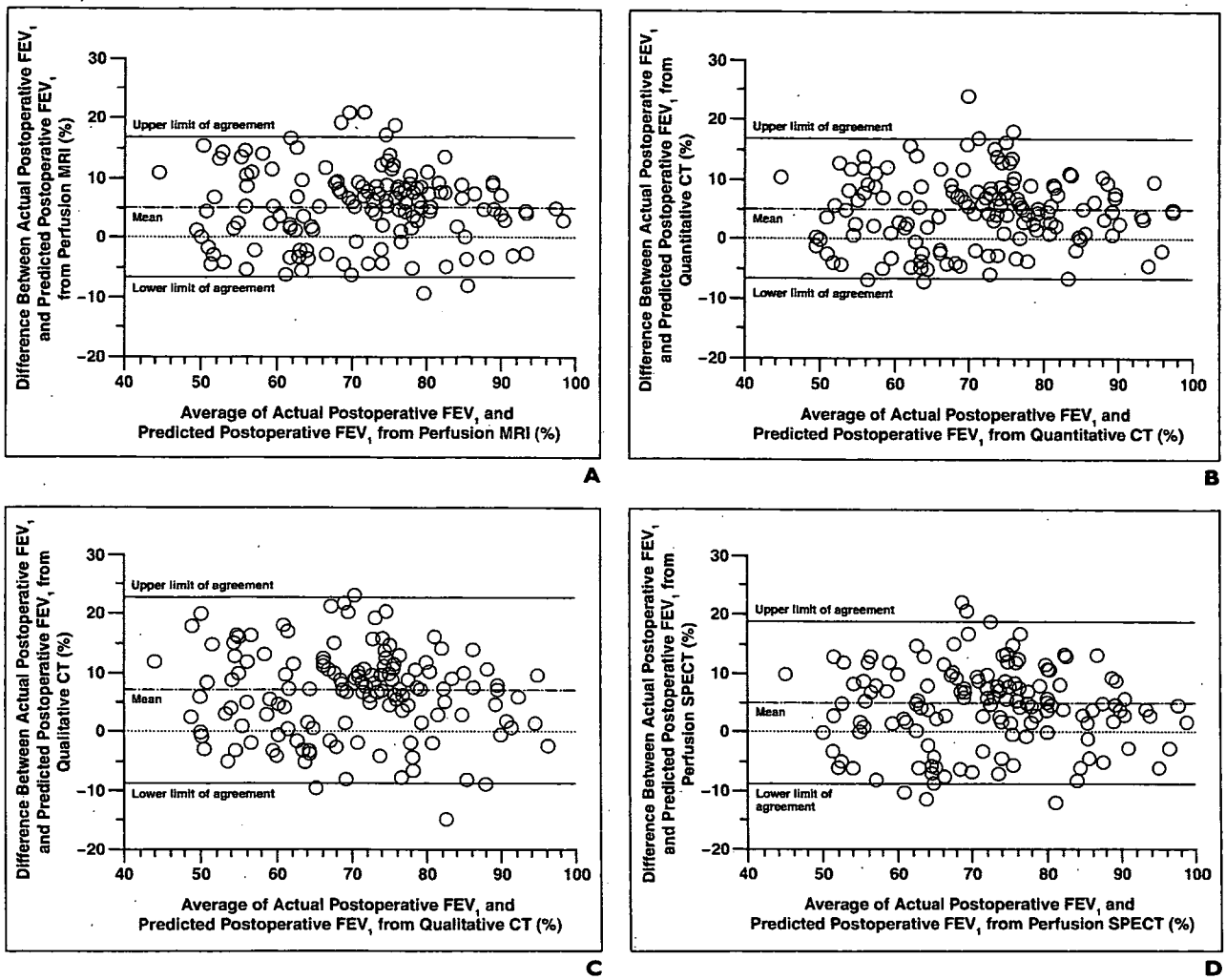

Fig. 3—The limits of agreement between actual postoperative forced expiratory volume in first second of expiration (FEV_1), expressed as percentage of predicted value, and each version of predicted postoperative FEV_1.
A, Graph shows the limits of agreement are 5.3% ± 11.8% for perfusion MRI.
B, Graph shows the limits of agreement are 5.0% ± 11.6% for quantitative assessment of CT scans.
C, Graph shows the limits of agreement are 6.8% ± 14.4% for qualitative assessment of CT scans.
D, Graph shows the limits of agreement are 5.1% ± 14.0% for perfusion SPECT.

quantitative assessment conducted with gadolinium contrast medium. Although indicator dilution theories are frequently used to determine regional blood volume and regional blood flow by means of various perfusion MRI techniques, direct application of these principles to contrast-enhanced, first-pass dynamic perfusion MRI experiments is difficult. Although regional blood volume can be determined by direct calculation of the area under the observed tissue–concentration curve, determination of calculated regional blood flow and mean transit time is less straightforward. Weisskoff et al. [28] pointed out that the use of the central volume principle to calculate mean transit time for locations within a tissue volume is inappropriate because changes in MRI signal intensity for specific tissue ROIs reflect the tracer concentration remaining in the tissue rather than that leaving the tissue. In addition, the observed signal intensity is assumed to be linearly related to the concentration of contrast medium within blood. Theoretically, this relation is not linear, but over a limited range of contrast concentrations it appears to be sufficiently linear to make the method valid [29]. Moreover, with use of the model it is assumed that the contrast agent remains within the intravascular space [30]. To the extent that the contrast agent acts as a purely intravascular marker, the volume of its distribution reflects blood volume. Therefore, despite the limitations, indicator dilution techniques with gadolinium contrast media can provide valid measures of regional pulmonary perfusion parameters.

A third limitation was associated with the fact that lung resection can improve the postoperative pulmonary function of patients with severe emphysema in the same way as does lung volume reduction surgery. The resultant beneficial effects on elastic recoil of

the lung and chest wall mechanics make it difficult to accurately predict postoperative lung function [31, 32]. It is therefore necessary for lung cancer patients with severe emphysema to undergo exercise lung function tests before lung resection for evaluation of their cardiopulmonary reserve, even though dynamic perfusion MRI and other radiologic methods are more accurate in prediction of postoperative lung function.

A fourth limitation was that the physiologic index and outcome were assessed 24–48 weeks postoperatively, not at a specified time. This factor affected the determination of actual postoperative lung function and the statistical comparison of predicted and actual postoperative lung function. Fifth, for quantitative assessment of functional lung from chest CT images of the entire lung, we had to use 5-mm slices because of the performance limitations of the computer. It would have been better to use images obtained in thinner sections for assessment of pulmonary emphysema. This disadvantage is a potential limitation for preoperative assessment of regional and total functional lung volume and estimation of postoperative lung function by means of quantitative CT assessment.

A sixth limitation was that we used commercially available software for prediction of postoperative lung function with quantitative CT and perfusion SPECT but used proprietary software for calculation of regional perfusion with dynamic perfusion MRI. Several proprietary software packages for quantitative assessment of regional perfusion parameters have been described [11, 15, 16, 19, 33, 34]. In this study, we did not compare the prediction error of our software with that of other software packages in analysis of data from the same patients. Further investigations are needed to determine the real statistical significance of our software for prediction of postoperative lung function.

A seventh limitation of this study was that we compared capabilities for prediction of postoperative lung function among dynamic perfusion MRI, quantitative and qualitative CT, and perfusion SPECT. We did not compare capabilities for prediction of other pulmonary functional parameters, such as static lung volume, diffusing capacity for oxygen, survival, quality of life, and cost-effectiveness. A prospective comparative study with a larger number of subjects may be warranted to determine the real importance in routine clinical practice of dynamic perfusion MRI as a substitute for quantitative and qualitative CT and perfusion SPECT or integrated SPECT and CT for prediction of the postoperative lung function of lung cancer patients.

In conclusion, dynamic perfusion MRI can be used to predict the postoperative lung function of lung cancer patients more accurately than qualitative CT and perfusion SPECT and at least as accurately as quantitative CT.

Acknowledgments

We thank Yoshiyuki Ohno, Professor Emeritus, Nagoya University (Department of Preventive Medicine, Graduate School of Medicine) for his advice on the statistical component of this study. We also thank Yoshimasa Maniwa (Division of Cardiovascular, Thoracic and Pediatric Surgery, Kobe University Graduate School of Medicine), and Yoshihiro Nishimura (Division of Cardiovascular and Respiratory Medicine, Department of Internal Medicine, Kobe University Graduate School of Medicine) for their contributions to this study.

References

1. Greenlee RT, Hill-Harmon MB, Murray T, Thun M. Cancer statistics, 2001. *CA Cancer J Clin* 2001; 51:15–36
2. Shields TW. Surgical therapy for carcinoma of the lung. *Clin Chest Med* 1993; 14:121–147
3. Pierce RJ, Copland JM, Sharpe K, Barter CE. Preoperative risk evaluation for lung cancer resection: predicted postoperative product as a predictor of surgical mortality. *Am J Respir Crit Care Med* 1994; 150:947–955
4. Bolliger CT, Jordan P, Soler M, et al. Exercise capacity as a predictor of postoperative complications in lung resection candidates. *Am J Respir Crit Care Med* 1995; 151:1472–1480
5. Wyser C, Stulz P, Soler M, et al. Prospective evaluation of an algorithm for the functional assessment of lung resection candidates. *Am J Respir Crit Care Med* 1999; 159:1450–1456
6. Olsen GN, Block AJ, Tobias JA. Prediction of postpneumonectomy pulmonary function using quantitative macroaggregate lung scanning. *Chest* 1974; 66:13–16
7. Markos J, Mullan BP, Hillman DR, et al. Preoperative assessment as a predictor of mortality and morbidity after lung resection. *Am Rev Respir Dis* 1989; 139:902–910
8. Giordano A, Calcagni ML, Meduri G, Valente S, Galli G. Perfusion lung scintigraphy for the prediction of postlobectomy residual pulmonary function. *Chest* 1997; 111:1542–1547
9. Bolliger CT, Guckel C, Engel H, et al. Prediction of functional reserves after lung resection: comparison between quantitative computed tomography, scintigraphy, and anatomy. *Respiration* 2002; 69:482–489
10. Wu MT, Pan HB, Chiang AA, et al. Prediction of postoperative lung function in patients with lung cancer: comparison of quantitative CT with perfusion scintigraphy. *AJR* 2002; 178:667–672
11. Ohno Y, Hatabu H, Higashino T, et al. Dynamic perfusion MRI versus perfusion scintigraphy: prediction of postoperative lung function in patients with lung cancer. *AJR* 2004; 182:73–78
12. Imaeda T, Kanematsu M, Asada S, et al. Prediction of pulmonary function after resection of primary lung cancer: utility of inhalation-perfusion SPECT imaging. *Clin Nucl Med* 1995; 20:792–799
13. Piai DB, Quagliatto R Jr, Toro I, Cunha Neto C, Etchbehere E, Camargo E. The use of SPECT in preoperative assessment of patients with lung cancer. *Eur Respir J* 2004; 24:258–262
14. Hatabu H, Gaa J, Kim D, Li W, Prasad PV, Edelman RR. Pulmonary perfusion: qualitative assessment with dynamic contrast-enhanced MRI using ultrashort TE and inversion recovery turbo FLASH. *Magn Reson Med* 1996; 36:503–508
15. Hatabu H, Tadamura E, Levin DL, et al. Quantitative assessment of pulmonary perfusion with dynamic contrast-enhanced MRI. *Magn Reson Med* 1999; 42:1033–1038
16. Levin DL, Chen Q, Zhang M, Edelman RR, Hatabu H. Evaluation of regional pulmonary perfusion using ultrafast magnetic resonance imaging. *Magn Reson Med* 2001; 46:166–171
17. Iwasawa T, Saito K, Ogawa N, Ishiwa N, Kurihara H. Prediction of postoperative pulmonary function using perfusion magnetic resonance imaging of the lung. *J Magn Reson Imaging* 2002; 15:685–692
18. Fink C, Puderbach M, Bock M, et al. Regional lung perfusion: assessment with partially parallel three-dimensional MR imaging. *Radiology* 2004; 231:175–184
19. Ohno Y, Hatabu H, Murase K, et al. Quantitative assessment of regional pulmonary perfusion in the entire lung using three-dimensional ultrafast dynamic contrast-enhanced magnetic resonance imaging: preliminary experience in 40 subjects. *J Magn Reson Imaging* 2004; 20: 353–365
20. Ohno Y, Hatabu H, Higashino T, et al. Oxygen-enhanced MR imaging: correlation with postsurgical lung function in patients with lung cancer. *Radiology* 2005; 236:704–711
21. Beccaria M, Corsico A, Fulgoni P, et al. Lung cancer resection: the prediction of postsurgical outcomes should include long-term functional results. *Chest* 2001; 120:37–42
22. Zeiher BG, Gross TJ, Kern JA, Lanza LA, Peterson MW. Predicting postoperative pulmonary function in patients undergoing lung resection. *Chest* 1995; 108:68–72

23. Kearney DJ, Lee TH, Reilly JJ, DeCamp MM, Sugarbaker DJ. Assessment of operative risk in patients undergoing lung resection: importance of predicted pulmonary function. *Chest* 1994; 105:753–759
24. Suga K, Kawakami Y, Zaki M, Yamashita T, Shimizu K, Matsunaga N. Clinical utility of co-registered respiratory-gated(99m)Tc-Technegas/MAA SPECT-CT images in the assessment of regional lung functional impairment in patients with lung cancer. *Eur J Nucl Med Mol Imaging* 2004; 31:1280–1290
25. [No authors listed]. Standardization of spirometry: 1987 update—statement of the American Thoracic Society. *Am Rev Respir Dis* 1987; 136:1285–1298
26. [No authors listed]. Lung function testing: selection of reference values and interpretative strategies. *Am Rev Respir Dis* 1991; 144:1202–1218
27. Bland JM, Altman DG. Statistical methods for assessing agreement between two methods of clinical measurement. *Lancet* 1986; 1:307–310
28. Weisskoff RM, Chesler D, Boxerman JL, Rosen BR. Pitfalls in MR measurement of tissue blood flow with intravascular tracers: which mean transit time? *Magn Reson Med* 1993; 29:553–558
29. Jerosch-Herold M, Wilke N, Stillman AE. Magnetic resonance quantification of the myocardial perfusion reserve with a Fermi function model for constrained deconvolution. *Med Phys* 1998; 25:73–84
30. Donahue KM, Weisskoff RM, Burstein D. Water diffusion and exchange as they influence contrast enhancement. *J Magn Reson Imaging* 1997; 7:102–110
31. Korst RJ, Ginsberg RJ, Ailawadi M, et al. Lobectomy improves ventilatory function in selected patients with severe COPD. *Ann Thorac Surg* 1998; 66:898–902
32. Sinjan EA, Van Schil PE, Ortmanns P, Van den Brande F, Hendriks JM, Eyskens E. Improved ventilatory function after combined operation for pulmonary emphysema and lung cancer. *Int Surg* 1999; 84:185–189
33. Nikolaou K, Schoenberg SO, Brix G, et al. Quantification of pulmonary blood flow and volume in healthy volunteers by dynamic contrast-enhanced magnetic resonance imaging using a parallel imaging technique. *Invest Radiol* 2004; 39:537–545
34. Risse F, Semmler W, Kauczor HU, Fink C. Dual-bolus approach to quantitative measurement of pulmonary perfusion by contrast-enhanced MRI. *J Magn Reson Imaging* 2006; 24:1284–1290

AJR WOMEN'S IMAGING

MRI Findings of Uterine Lipoleiomyoma Correlated with Pathologic Findings

Kazuhiro Kitajima[1,2]
Yasushi Kaji[1]
Kazufumi Imanaka[3]
Ryo Sugihara[2]
Kazuro Sugimura[2]

OBJECTIVE. Our objective was to describe the MRI findings of uterine lipoleiomyoma and to correlate them with histopathologic findings.

CONCLUSION. Uterine lipoleiomyoma typically presents as a well-demarcated mass showing hyperintensity with hypointense amorphous bundles on T1- and T2-weighted images with chemical shift artifacts. The hyperintense region suppressed on chemical shift fat-suppressed sequences and the hypointense bundles enhanced by contrast material pathologically correspond to mature fat tissue and smooth muscle tissue, respectively. Even in an atypical case with a small volume of fat tissue in the mass, a fat-suppression MRI sequence is especially useful for the diagnosis.

Keywords: lipoleiomyoma, MRI, myoma, uterine neoplasms

DOI:10.2214/AJR.07.2230

Received November 3, 2006; accepted after revision March 28, 2007.

[1]Department of Radiology, Dokkyo Medical University School of Medicine, Mibu, Japan. Address correspondence to K. Kitajima, 880 Kita-kobayashi, Mibu, Shimotuka-gun, Tochigi 321-0293, Japan (kazu10041976@yahoo.co.jp).

[2]Department of Radiology, Kobe University Graduate School of Medicine, Kobe, Japan.

[3]Department of Radiology, Nishi-Kobe Medical Center, Kobe, Japan.

WEB
This is a Web exclusive article.

CME
This article is available for CME credit. See www.arrs.org for more information.

AJR 2007; 189:W100–W104

0361–803X/07/1892–W100

Lipoleiomyoma of the uterus is a rare benign uterine tumor suspected of being a variation of leiomyoma [1, 2]. Histologically, uterine lipoleiomyoma consists of smooth muscle cells, mature adipose tissue, and fibrous tissue in various ratios. To our knowledge, no published compendium exists of the broad spectrum of MRI findings of this entity except for case reports. This study describes the MRI appearance of nine patients with uterine lipoleiomyoma (seven cases showing typical MRI findings noted in previous case reports and two cases showing atypical MRI findings with a small volume of fatty tissue) and correlates these imaging findings with the histopathologic findings.

Materials and Methods

Between 1997 and 2006, nine patients with surgically proven uterine lipoleiomyoma underwent pelvic MR examinations preoperatively in two institutions (Nishi-Kobe Medical Center and Kobe University Graduate School of Medicine). No ethics committee approval was required at these two institutes because the study was a retrospective review of clinical cases. The nine patients ranged in age from 47 to 76 years old (mean, 61 years), and seven patients (78%) were postmenopausal. Clinical presentation was abdominal pressure in four patients, irregular menstruation in three, dysuria in one, and anemia in one. Six patients underwent total abdominal hysterectomy with bilateral salpingo-oophorectomy and three patients underwent simple hysterectomy. Coexistence with other nonlipomatous leiomyomas was noted in six patients. We retrospectively reviewed the clinical records and MRI findings of the nine patients and correlated these MRI findings with histopathologic findings.

MRI was performed with a 1.5-T superconducting magnet (Magnetom Vision or Symphony, Siemens Medical Solutions [$n = 5$ patients]; or Gyroscan Intera, Philips Medical Systems [$n = 4$ patients]) using a phased-array coil. The slice thickness was 4–6 mm, intersection gap was 1 mm, field-of-view measurements were 24–33 cm, and matrix size was 192 × 256–256 × 512. The number of signal averages was 1 or 2. A conventional spin-echo technique was used to obtain T1-weighted images (TR range/TE range, 500–650/9–13) and a turbo spin-echo technique (3,500–4,000/91–106) to obtain T2-weighted images. The echo-train length ranged from 5 to 10. Sagittal and axial T1- and T2-weighted images were obtained for all patients. The axial images were obtained on the body axis, not on the uterine axis, in most patients. Sagittal or axial chemical shift selective (CHESS) T1-weighted images were obtained for all patients. Immediately after the IV injection of 0.1 mmol/kg of body weight of gadopentetate dimeglumine (Magnevist, Schering), CHESS T1-weighted images were obtained in four patients. To reduce peristalsis, 1 mL of butylscopolamine (Buscopan, Boehringer Ingelheim) was administered intramuscularly before the examination unless contraindicated.

MRI findings were interpreted with only knowledge of the pathologic diagnosis of uterine lipoleiomyoma; two radiologists attained consensus regarding the appearance of the lesion, including the size, location, growth pattern, signal intensity,

TABLE 1: Characteristics of Uterine Lipoleiomyomas in Nine Patients

Patient No.	Age (y)	Symptom	Location	Size (cm)	Other Myomas Present	MRI Signal Intensity	
						T1-Weighted	T2-Weighted
1	55	Irregular menstruation	Intramural corpus	5.5 × 6.0	Yes	Hyperintense with hypointense bands	Hyperintense with hypointense bands
2	70	Dysuria	Subserosal corpus	6.0 × 6.5	Yes	Hyperintense with hypointense bands	Hyperintense with hypointense bands
3	65	Abdominal pressure	Intramural corpus	8.5 × 9.0	Yes	Hyperintense with hypointense amorphous area	Hyperintense with hypointense amorphous area
4	55	Anemia	Intramural corpus	4.0 × 4.5	No	Hyperintense with hypointense amorphous area	Hyperintense with hypointense amorphous area
5	49	Irregular menstruation	Intramural corpus	2.5 × 3.5	No	Hyperintense with hypointense amorphous area	Hyperintense with hypointense amorphous area
6	64	Irregular menstruation	Intramural corpus	5.5 × 7.0	Yes	Hyperintense with hypointense amorphous area	Hyperintense with hypointense amorphous area
7	76	Abdominal pressure	Subserosal corpus	8.0 × 11.0	Yes	Hyperintense with hypointense amorphous area	Hyperintense with hypointense amorphous area
8	64	Abdominal pressure	Intramural corpus	9.0 × 10.0	No	Hypointense with slightly hyperintense area and very hyperintense spots	Mixed hypo- and hyperintense
9	47	Abdominal pressure	Subserosal corpus	9.0 × 10.0	Yes	Slightly hypointense with hyperintense spots	Heterogeneously hyperintense

Note—Patient 1 is shown in Figure 1, patient 3 in Figure 2, and patient 8 in Figure 3.

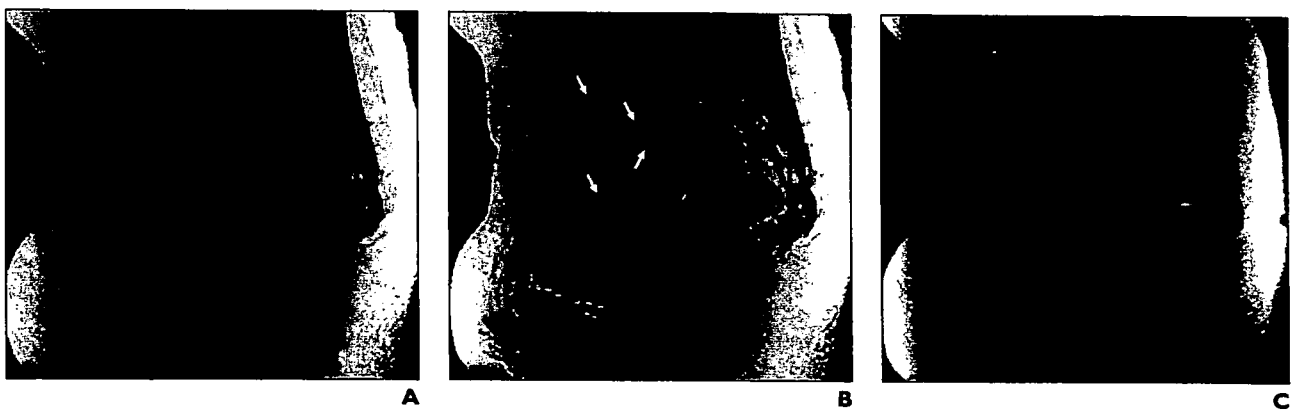

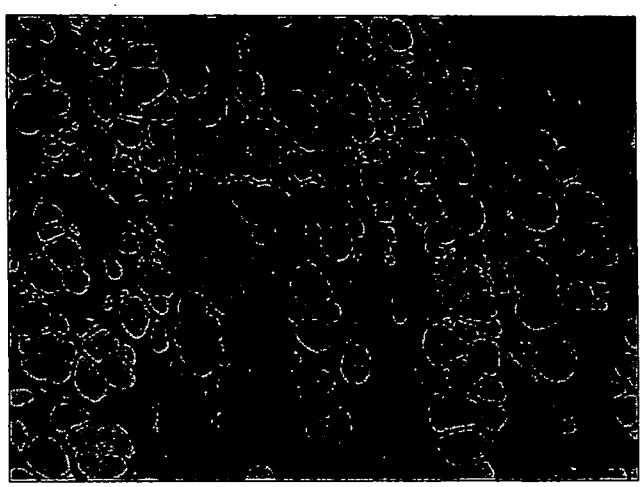

Fig. 1—55-year-old woman with irregular menstruation (typical case).
A, Sagittal spin-echo T1-weighted MR image (TR/TE, 530/10) shows 55 × 60 mm, well-circumscribed mass in myometrium of corpus uteri as hyperintense with hypointense bands.
B, Sagittal turbo spin-echo T2-weighted MR image (3,570/93) shows mass as hyperintense with hypointense bands and chemical shift artifact along frequency direction in mass (*arrows*).
C, Fat-suppression chemical shift selective sagittal spin-echo T1-weighted MR image (530/10) shows signal suppression of hyperintense region on T1-weighted image (**A**).
D, Macrograph of resected specimen shows abundant mature lipocytes intermixed with smooth muscle cells.

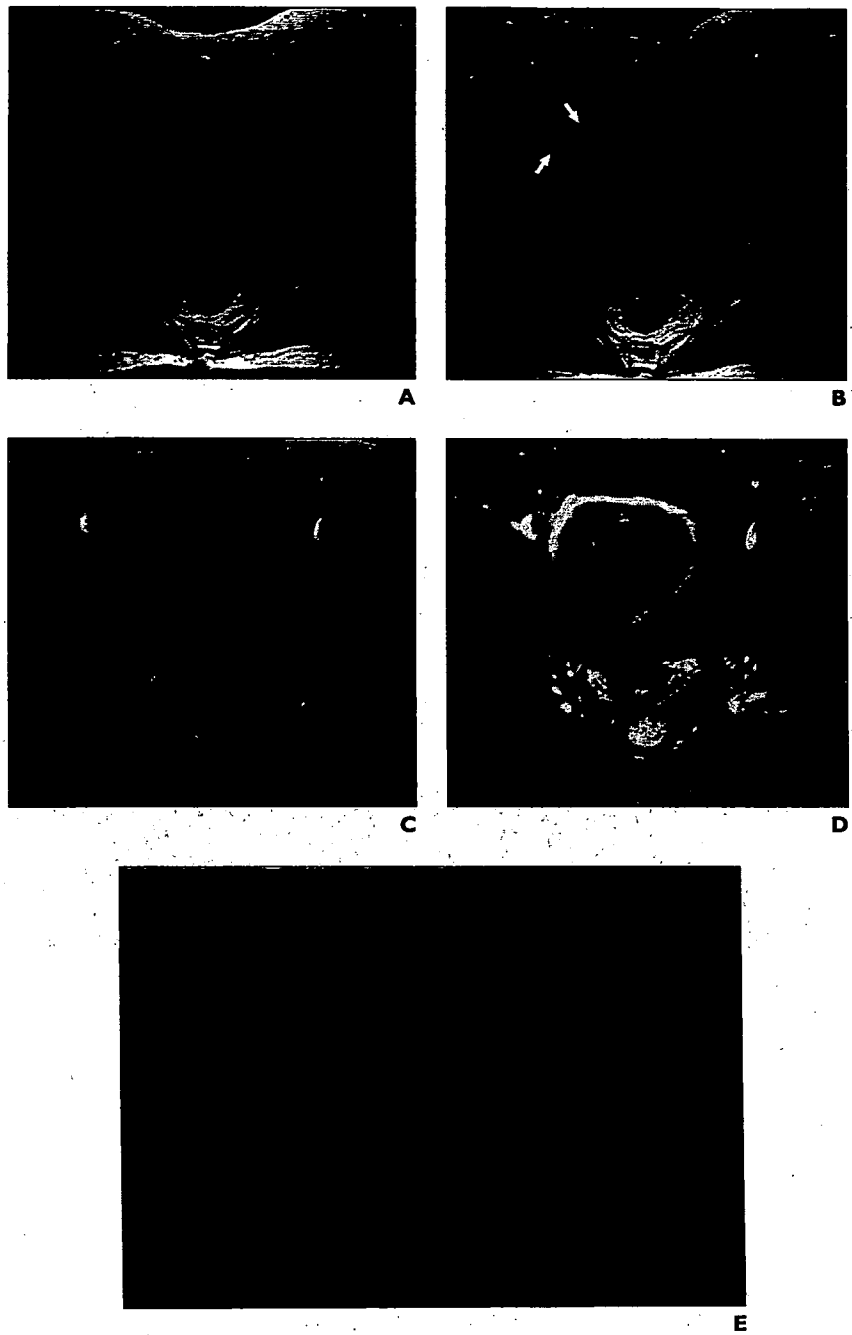

Fig. 2—65-year-old woman with abdominal pressure (typical case).
A, Axial spin-echo T1-weighted MR image (TR/TE, 600/13) shows 85 × 90 mm, well-circumscribed mass in myometrium of corpus uteri as hyperintense with hypointense amorphous bands.
B, Axial turbo spin-echo T2-weighted MR image (4,000/106) shows mass as hyperintense with hypointense amorphous bands and chemical shift artifact along frequency direction in mass (*arrows*).
C, Fat-suppression chemical shift selective axial spin-echo T1-weighted MR image (500/13) shows signal suppression of hyperintense region on T1-weighted image (A).
D, Fat-suppressed, gadolinium-enhanced axial spin-echo T1-weighted MR image (500/13) shows strong enhancement of amorphous bands.
E, Macrograph of resected specimen shows abundant mature lipocytes intermixed with smooth muscle cells.

chemical shift artifact, and the presence of fat and hemorrhage. The signal intensity of the lesion was rated on both T1- and T2-weighted images as low intensity, isointensity, or high intensity relative to the signal intensity of the myometrium. These radiologic findings were grossly and micropathologically correlated with pathologic findings.

Results

The MRI appearances of nine patients with uterine lipoleiomyoma are summarized in Table 1. The maximal diameter of the tumors ranged from 3.5 to 11 cm (mean, 7.5 cm). All the lesions were well circumscribed. Tumor location was the myometrium of the uterine corpus in six patients and the subserosa of the uterine corpus in three. On T1-weighted images, the lesions exhibited hyperintensity with hypointense amorphous bands in seven patients (Figs. 1 and 2) and slight hypointensity with hyperintense spots in two patients (Fig. 3). All hyperintense areas on T1-weighted images, which were suppressed on CHESS sequences, reflected fat tissue pathologically. On T2-weighted images, the lesions exhibited hyperintensity with hypointense amorphous bands in seven patients (Figs. 1 and 2), a mixture of heterogeneously hypo- and hyperintensity in one patient (Fig. 3), and heterogeneous hyperintensity in one patient. These hypointense and hyperintense areas on T2-weighted image in patient 8 reflected pathologically stromal hyalinization and stromal edematous change, respectively. This heterogeneously hyperintense region on T2-weighted images in patient 9 reflected stromal myxomatous change. T2-weighted images showed chemical shift artifact along the frequency direction in the mass in four (45%) of nine patients (Figs. 1–3). The hypointense areas on T1- and T2-weighted images in four patients were strongly enhanced by contrast material (Fig. 2), reflecting smooth muscle or fibrous tissue pathologically.

Discussion

Lipomatous uterine tumors are uncommon. Approximately 180 cases have been reported in the literature. According to previous reports, the incidence ranged from 0.03% in hysterectomy specimens to 0.20% in uterine leiomyomas [1, 2]. Pathologically, lipomatous uterine tumors have been categorized into three groups [3, 4]. The first group is pure lipoma, which is composed of mature fat cells only and is encapsulated [5]. The second group consists of lipoleiomyoma [6–9], angiomyolipoma [10], fibromyolipoma [11], and

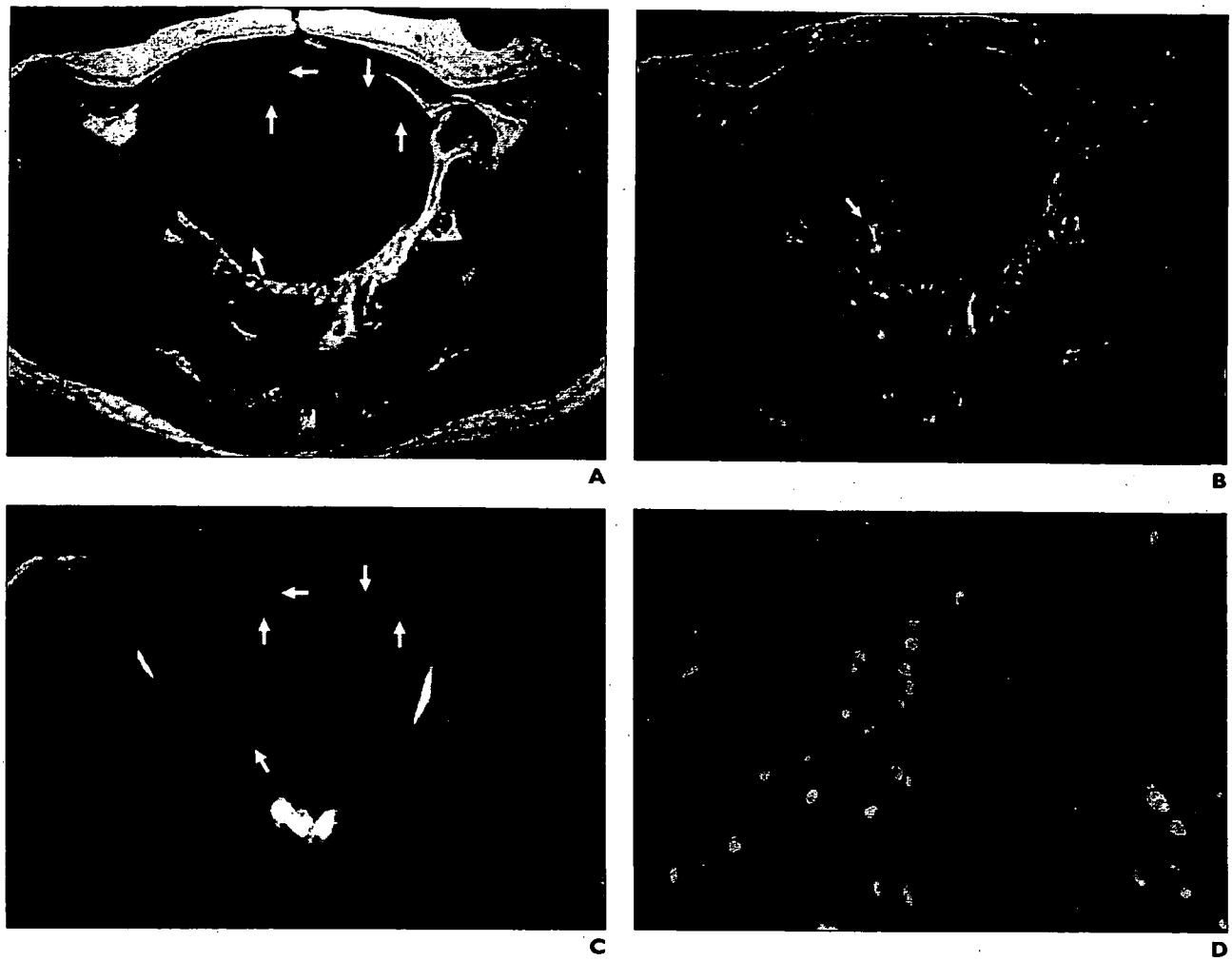

Fig. 3—64-year-old woman with abdominal pressure (atypical case).
A, Axial spin-echo T1-weighted MR image (TR/TE, 650/12) shows 9 × 10 cm, well-circumscribed mass in myometrium of corpus uteri as slightly hypointense with slightly hyperintense area and very hyperintense spots (*arrows*).
B, Axial turbo spin-echo T2-weighted MR image (3,500/96) shows mass as heterogeneously mixed hypo- and hyperintensity and chemical shift artifact along frequency direction in mass (*arrow*).
C, Fat-suppressed chemical shift selective axial spin-echo T1-weighted MR image (650/12) shows signal suppression of very hyperintense spots (*arrows*) on T1-weighted image (**A**).
D, Macrograph of resected specimen shows smooth muscle cells intermixed with small volume of mature lipocytes.

so on; that is, mixed tumors containing various mesodermal tissue components such as adipose fat, smooth muscle cells, a fibrous component, and connective tissue. These neoplasms are also well-encapsulated benign growths. The third and rarest group is malignant neoplasm, liposarcoma, which consists of less-differentiated fat cells that have undergone sarcomatous change [12]. Lipoleiomyoma is the most common entity in these three categories. Although the origin of lipomatous lesions of the uterus has been the subject of much speculation, three theories are common: direct metaplasia of smooth muscle or connective tissue into fat cells, differentiation from misplaced embryonic fat cells, and proliferation of accompanying perivascular fat cells into the blood vessels [2, 3].

Uterine lipoleiomyoma occurs most frequently in postmenopausal women from 50 to 70 years old. This entity has been reported to range from 3 mm to 32 cm in diameter (average, between 5 and 10 cm). It is usually well circumscribed with a thin connective-tissue capsule. It is most frequently located in the posterior wall of the uterine corpus; 10% or more are also seen in the uterine cervix. This lesion is often associated with common leiomyomas [1–4].

Several case reports have described the MRI finding of uterine lipoleiomyoma, and all reports described typical cases containing abundant fat tissue in the mass [6–9]. This entity typically presents as a well-demarcated mass that is hyperintense with hypointense amorphous bundles on T1- and T2-weighted

images with chemical shift artifact. The hyperintense region is suppressed on CHESS sequences. The MRI characteristics observed in our series were variable and depended on the volume of mesodermal tissue such as fat, muscle, connective tissue, and stromal degeneration making up the lesion. Seven (78%) of nine cases with abundant fat tissue in the mass presented typical MRI findings as described in previous reports.

However, two cases (22%) with a small volume of fat tissue showed slight hypointensity with a small hyperintense area on T1-weighted images and various signal intensities on T2-weighted images because the stroma of the lesion showed various degeneration. Even in these two atypical cases, CHESS imaging was useful for the identification of a small fat component. Double-echo gradient-echo chemical shift MRI (in-phase and opposed-phase imaging), which was not used in our series, may also be useful to detect a small volume of fat in the mass [13]. Because the presence of a hyperintense area in the uterine mass on T1-weighted images is usually associated with hemorrhage in uterine leiomyosarcoma, a fat-suppression MRI sequence is important because of its ability to differentiate fat tissue and hemorrhage.

Our study has some limitations because of its retrospective nature, small sample size, and use of two types of MR equipment. The axial images were obtained on the body axis, not on the uterine axis, in most patients. In this context, further study should be conducted.

In conclusion, MRI including a fat-suppression sequence is a useful technique to diagnose uterine lipoleiomyoma, with its high sensitivity and specificity to fat and with its multisectional ability to show the precise location of the lesion. Although it is not always possible to differentiate uterine lipoleiomyoma from other uterine lipomatous tumors (angiomyolipoma, fibromyolipoma, myelolipoma, liposarcoma, and so on) on MRI, it is important to become familiar with the wide variety of MRI findings of this entity because a correct preoperative diagnosis is critical to determine appropriate treatment and to avoid unnecessary intervention.

References

1. Silverberg SG, Kurman RJ. *Tumors of the uterine corpus and gestational trophoblastic disease.* Washington, DC: Armed Forces Institute of Pathology, 1992:127–130
2. Brandfass RT, Everts-Suarez EA. Lipomatous tumors of the uterus: a review of the world's literature with report of a case of true lipoma. *Am J Obstet Gynecol* 1955; 70:359–367
3. Willen R, Gad A, Willen H. Lipomatous lesions of the uterus. *Virchows Arch A Pathol Anat Histol* 1978; 377:351–361
4. Chachutow D, Brill R. Lipomas of uterus. *Am J Obstet Gynecol* 1957; 73:1358–1361
5. Lau LU, Thoeni RF. Uterine lipoma: advantage of MRI over ultrasound. *Br J Radiol* 2005; 78:72–74
6. Dodd GD III, Budzik RF Jr. Lipomatous uterine tumors: diagnosis by ultrasound, CT, and MR. *J Comput Assist Tomogr* 1990; 14:629–632
7. Tsushima Y, Kita T, Yamamoto K. Uterine lipoleiomyoma: MRI, CT and ultrasonographic findings. *Br J Radiol* 1997; 70:1068–1070
8. Ishigami K, Yoshimitsu K, Honda H, et al. Uterine lipoleiomyoma: MRI appearances. *Abdom Imaging* 1998; 23:214–216
9. Maebayashi T, Imai K, Takekawa Y, et al. Radiologic features of uterine lipoleiomyoma. *J Comput Assist Tomogr* 2003; 27:162–165
10. Yaegashi H, Moriya T, Soeda S, et al. Uterine angiomyolipoma: case report and review of the literature. *Pathol Int* 2001; 51:896–901
11. Soyer P, Harry G, Cazier A, Masselot J, Vanel D. Uterine fibromyolipoma: uncommon imaging features. *Eur J Radiol* 1991; 13:67–68
12. Scurry J, Hack M. Leiomyosarcoma arising in a lipoleiomyoma. *Gynecol Oncol* 1990; 39:381–383
13. Outwater EK, Blasbalg R, Siegelman ES, et al. Detection of lipid in abdominal tissue with opposed-phase gradient-echo images at 1.5T: techniques and diagnostic importance. *RadioGraphics* 1998; 18:1465–14

Radiat Med (2007) 25:346–354
DOI 10.1007/s11604-007-0151-5

ORIGINAL ARTICLE

Magnetic resonance imaging findings of endometrioid adenocarcinoma of the ovary

Kazuhiro Kitajima · Yasushi Kaji · Yoichiro Kuwata
Kazufumi Imanaka · Ryo Sugihara · Kazuro Sugimura

Received: December 25, 2006 / Accepted: April 13, 2007

Abstract
Purpose. We assessed magnetic resonance imaging (MRI) features and clinical characteristics of ovarian endometrioid adenocarcinoma.
Materials and methods. A total of 31 patients with 39 surgically proven ovarian endometrioid adenocarcinomas were analyzed retrospectively. Histologically, 13 lesions in 12 patients arose from proven endometriomas (group A), and 26 lesions in 19 patients did not coexist with endometrioma (group B). The morphological pattern of the lesion on MRI was classified as a solid or a cystic type: A solid type was defined as a solid component occupying more than half of the lesion; and a cystic type was a cystic lesion with one or more mural nodules.
Results. Altogether, 11 lesions in group A were the cystic type on MRI, whereas 24 lesions in group B were the solid type ($P < 0.0001$). Among the 11 cystic-type lesions in group A, the cysts of 5 lesions were hypointense on T1-weighted images, and the cysts of 6 lesions were hyperintense on T1- and T2-weighted images without "shading." The nuclear grade was higher ($P = 0.0028$) and the clinical stage more advanced ($P = 0.0018$) in group B compared to group A.
Conclusion. MRI of ovarian endometrioid adenocarcinomas revealed two types: a solid type and a cystic type. The lesions arising from endometriomas tended to be the cystic type on MRI and have a good prognosis. Preexisting endometrioma in this entity rarely showed "shading" on T2-weighted images.

Key words Ovary · Neoplasms · Endometrioid carcinoma · Endometrioma · Magnetic resonance imaging (MRI)

K. Kitajima (✉) · Y. Kaji
Department of Radiology, Dokkyo Medical University School of Medicine, 880 Kita-kobayashi, Mibu, Shimotuka-gun, Tochigi 321-0293, Japan
Tel. +81-282-86-1111; Fax +81-282-86-4940
e-mail: kazu10041976@yahoo.co.jp

Y. Kuwata · K. Imanaka
Department of Radiology, Nishi-Kobe Medical Center, Kobe, Japan

K. Kitajima · R. Sugihara · K. Sugimura
Department of Radiology, Kobe University Graduate School of Medicine, Kobe, Japan

Introduction

Endometrioid adenocarcinoma of the ovary is defined as a primary ovarian surface epithelial carcinoma that is histologically identical to typical endometrial adenocarcinoma, comprising 5.7% of ovarian surface epithelial neoplasms, 17.5% of ovarian carcinomas, and 93.0% of endometrioid ovarian neoplasms.[1,2] This entity was described in 1925 by Sampson, who insisted that endometriosis may serve as a possible source of ovarian carcinoma and that endometrial-like carcinoma, in particular, may arise either from endometriosis or de novo from the ovarian surface.[3] The World Health Organization in 1964 recognized the term "endometrioid carcinoma of the ovary."[4] The incidence of endometrioma coexisting with ovarian endometrioid adenocarcinoma is reported to range from 15% to 25%.[1,2,5]

The most common histological type of ovarian carcinoma arising in ovarian endometrioma is clear cell carcinoma, and there is one report that discusses magnetic

resonance imaging (MRI) of ovarian clear cell carcinoma.[6] We found only two Japanese reports describing MRI findings of ovarian endometrioid adenocarcinoma,[7,8] and MRI findings of this entity have not been fully described in the English literature. We compared MRI findings (tumor number, size, morphological pattern, signal intensity, uterine findings, ascites) and clinical manifestations (age, tumor nuclear grade, pathologically proven uterine carcinoma, ascites, clinical stage) of 39 histologically proven ovarian endometrioid adenocarcinomas with and without pathologically proven endometrioma.

Materials and methods

Patients

Between 1998 and 2005, a total of 31 patients with 39 surgically and pathologically proven primary ovarian endometrioid adenocarcinomas underwent MRI examinations preoperatively in two institutions (Nishi-Kobe Medical Center and Kobe University Graduate School of Medicine) and had not received preoperative chemotherapy. Five patients receiving preoperative chemotherapy for ovarian endometrioid adenocarcinoma in Kobe University Graduate School of Medicine during the same years were excluded from this study. There was no ethics committee approval of this study required at these two institutions because this study is a retrospective review of clinical cases. Radical surgery at the two centers was performed within 2 weeks after MRI in all cases.

Methods

MRI was performed with a 1.5-T superconducting magnet (Magnetom Vision, or Symphony; Siemens, Erlangen, Germany) in 21 patients and a 1.5-T superconducting magnet (Gyroscan Intera; Philips, Best, The Netherlands) in 10 patients using a phased-array coil. The slice thickness was 5–6 mm, intersection gap was 1 mm, field-of-view measurements were 24–33 cm, matrix size was 192 × 256 to 256 × 512. A conventional spin-echo technique was used to obtain T1-weighted images (TR/TE ranges: 510–610/9–12), and turbo spin-echo techniques (3000–3510/88–96) were used to obtain T2-weighted images. The echo train length ranged from 5 to 10. Immediately after intravenous injection of gadopentetate dimeglumine 0.1 mmol/kg body weight (Magnevist; Schering, Berlin, Germany), T1-weighted fat-suppression conventional SE images were obtained in 26 patients. All images were obtained in both axial and sagittal planes. To reduce peristalsis, 1 ml of a butylscopolamine (Buscopan; Boehringer Ingelheim, Ingelheim am Rhein, Germany) was administered intramuscularly before the examination unless contraindicated.

The MRI findings were interpreted by two experienced radiologists (Y.K. with 15 years and K.K with 5 years of experience with pelvic MRI) who knew only the pathological diagnosis of ovarian endometrioid carcinoma; the radiologists attained consensus regarding the tumor number, size, morphological appearance, signal intensity, and uterine findings and ascites. On MRI, the primary lesion was morphologically described as a cystic type or solid type. The cystic type consisted of three subgroups: unilocular cyst with a monomural nodule, unilocular cyst with multimural nodules, and multilocular cyst with multimural nodules. The solid type was visually and roughly defined as having a solid component that occupied more than half of the entire lesion. The signal intensity of the lesion was compared with that of myometrium on T1-weighted images and compared with that of outer myometrium on T2-weighted images. "Very high" signal intensities on T1- and T2- weighted images indicated intensities equal to those of fat and urine, respectively.

Statistical analysis

Differences between several factors—such as age, clinical stage, ascites, coexistence of uterine carcinoma, tumor size, morphological pattern, nuclear grade—in the two groups were analyzed by Fisher's test or the Mann-Whitney test as appropriate. $P < 0.05$ was regarded as statistically significant.

Results

Patients ranged from 31 to 67 years old (mean 51 years), and 18 patients (58%) were postmenopausal. Altogether, 14 patients had abdominal distension, 10 had lower abdominal pain, 4 had irregular menstruation, and 3 patients were asymptomatic. Cancer antigen CA 125 levels were elevated in 20 of 25 patients (80%); cancer antigen CA 19-9 levels were elevated in 13 of 26 patients (50%); and carcinoembryonic antigen (CEA) levels were elevated in 3 of 27 patients (11%). Of the lesions, 10 involved the right ovary, 13 involved the left, and 8 showed bilateral involvement. The tumor nuclear grade (G) of the 39 lesions was G1 in 8, G2 in 7, and G3 in 24. Altogether, 13 lesions in 12 patients originated from histologically proven endometrioma (39%). Five patients had histologically proven uterine carcinoma (16%). The International Federation of Gynecology and Obstetrics

Table 1. Classification of 31 patients with ovarian endometrioid adenocarcinoma according to ovarian endometrioma

Parameter	Ovarian endometrioid carcinoma		*P*
	Group A with endometrioma	Group B without endometrioma	
No. of patients	12	19	
Age (years), mean ± SD and range	57.8 ± 7.2 (45–67)	52.7 ± 10.8 (31–69)	0.2074
No. of tumors	13	26	0.1082
Tumor size (cm)	10.8 ± 4.3	9.4 ± 3.7	0.4411
Tumor morphological pattern (cystic/solid) on MR	11/2	2/24	<0.0001**
Tumor nuclear grade (G1:G2:G3)	6:3:4	2:4:20	0.0028*
Coexistence of uterine carcinoma	0	5	0.0588
Ascites: benign/malignant	4/5	5/14	0.4074
FIGO stage			0.0018*
I	9 (75%)	1 (5%)	
II	0	7 (37%)	
III	3 (25%)	8 (42%)	
IV	0	3 (16%)	
Total	12 (100%)	19 (100%)	

Group A, patients having ovarian endometrioid carcinoma arising from endometrioma
Group B, patients having ovarian endometrioid carcinoma without endometrioma
* $P < 0.05$ by Mann-Whitney test
** $P < 0.001$ by Fisher test

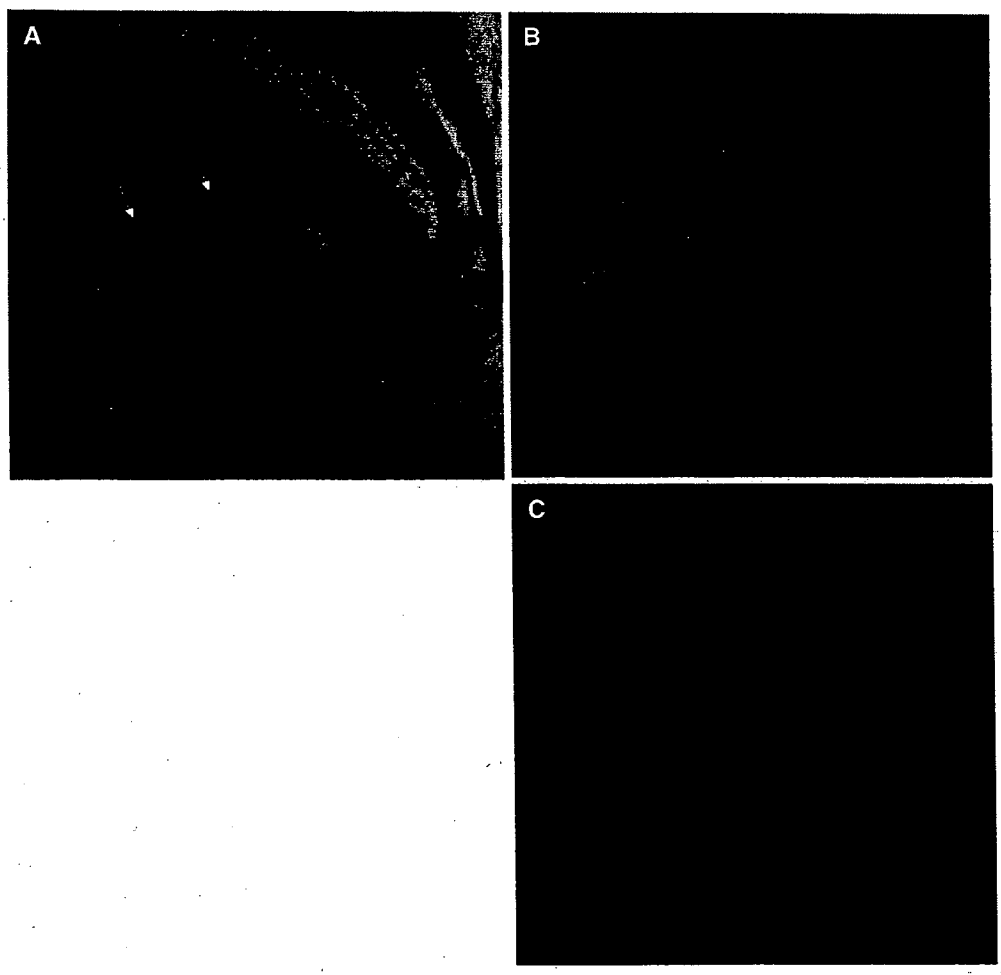

Fig. 1. A 55-year-old woman of pT1aN0M0 (grade 2) with a preexisting endometrioma. **A** Sagittal spin-echo T1-weighted magnetic resonance (MR) image (600/12) shows a 7-cm hypointense unilocular cystic mass with a 4-cm, isointense mural nodule (*arrows*). **B** Sagittal turbo spin-echo T2-weighted MR image (3400/92) shows a very hyperintense unilocular cyst with a hypo- and hyperintense mixed mural nodule. **C** Fat suppression, gadolinium-enhanced sagittal spin-echo T1-weighted MR image (600/12) shows strong enhancement of the mural nodule with a central nonenhanced necrotic region

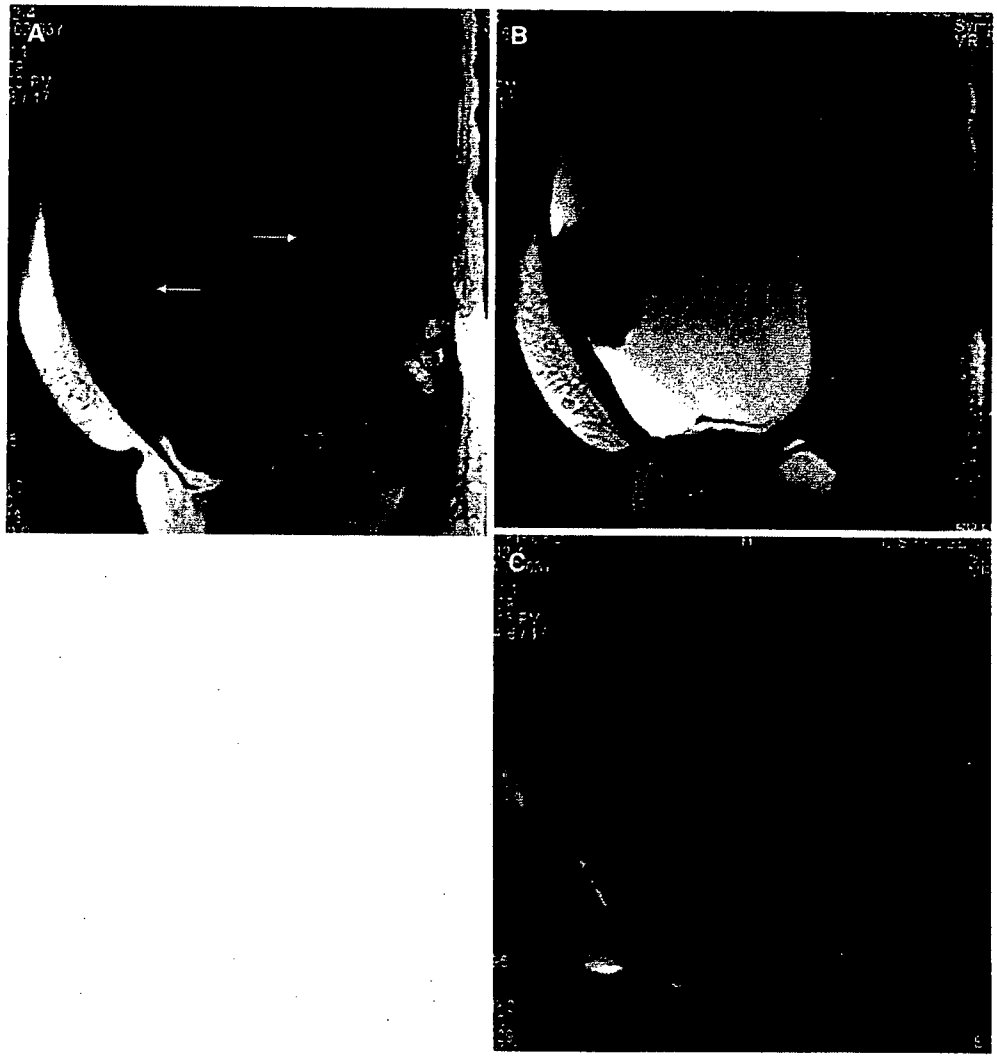

Fig. 2. A 63-year-old woman of pT1cN0M0 (grade 1) with a preexisting endometrioma. **A** Sagittal spin-echo T1-weighted MR image (600/12) shows a 20-cm hypointense unilocular cystic mass with multiple isointense mural nodules (*arrows*), the largest of which measured 6 cm in diameter. **B** Sagittal turbo spin-echo T2-weighted (3500/92) MR image shows a very hyperintense unilocular cystic mass with multiple isointense mural nodules. **C** Fat suppression, gadolinium-enhanced sagittal spin-echo T1-weighted MR image (600/12) shows strong enhancement of the mural nodules

staging (1998) and pTNM classification of 31 patients were stage I in 10 patients (pT1aN0M0 in seven, pT1cN0M0 in three), stage II in 7 (pT2aN0M0 in one, pT2bN0M0 in three, pT2cN0M0 in three), stage III in 11 (pT3bN0M0 in five, pT3cN0M0 in four, pT3bN1M0 in one, pT3cN1M0 in one), and stage IV in three (pT2cN0M1 in one, pT3bN0M1 in one, pT3cN1M1 in one).

The relations of clinical factors and MRI findings between carcinomas arising from endometrioma (group A) and carcinomas without endometrioma (group B) are listed in Table 1. The nuclear grade is higher in group B ($P = 0.0028$, Mann-Whitney test), and the clinical stage is more advanced in group B ($P = 0.0018$, Mann-Whitney test) compared to group A. Uterine endometrial carcinoma was pathologically confirmed in five patients in group B but not in group A. Although 9 of 12 patients in group A and all 19 patients in group B had ascites on MRI, cytologically 9 cases (4 in group A and 5 in group B) were benign and 19 cases (5 in group A and 14 in group B) were malignant. Group A lesions tended to be the cystic type, and group B lesions tended to be the solid type on MRI ($P < 0.0001$, Fisher's test).

The MRI findings for 13 carcinomas in group A morphologically were the cystic type in 11 lesions (Figs. 1, 2) and the solid type in 2 lesions (Table 2). These 11 cystic lesions consisted of unilocular cystic lesions with monomural nodules in three (Fig. 1), unilocular cystic lesions with multimural nodules in four (Fig. 2), and multilocular cystic lesion with multi-mural nodules in four. The signal intensity of cystic components in these 11 cystic lesions on T1-weighted images was low in five (Figs. 1, 2), slightly high in two, variably low to high in three, and very high in one; on T2-weighted images, the

Table 2. MRI findings of ovarian endometrioid adenocarcinomas of 39 lesions in 31 patients

Parameter	Group I with endometrioma		Group II without endometrioma	
	Cystic	Solid	Cystic	Solid
No. of tumors	11	2	2	24
Morphological pattern of cystic type				
Unilocular cyst with monomural nodule	3		0	
Unilocular cyst with multimural nodules	4		0	
Multilocular cyst with multimural nodules	4		2	
Signal intensity of large cyst on T1-weighted image				
Low	5		0	
Slightly high	2		1	
Variable from low to high	3		0	
Very high	1		1	
Signal intensity of large cyst on T2-weighted images				
High	2		0	
Very high	9		2	
Maximum diameter of mural nodule (cm)				
≤2.0	2		0	
>2.0 and ≤4.0	6		0	
>4.0 and ≤6.0	2		1	
>6.0	1		1	
Signal intensity of mural nodules on T1-weighted images				
Low	2		1	
Intermediate	9		1	
Signal intensity of mural nodules on T2-weighted images				
Low	1		0	
Intermediate	3		1	
Slightly high	3		0	
Low and high mixed	4		1	
Signal intensity of solid component on T1-weighted images				
Low		0		1
Intermediate		1		20
Intermediate and high mixed		1		3
Signal intensity of solid component on T2-weighted images				
Intermediate		0		1
Heterogeneous intermediate		1		5
Slightly high		0		4
Low and mixed		0		3
Heterogeneous high		1		11

MRI, magnetic resonance imaging

signal intensity was high in two and very high in nine (Figs. 1, 2). The maximum size of the mural nodules was 2 cm in two, 3 cm in three, 4 cm in three (Fig. 1), 5 cm in one, 6 cm in one (Fig. 2), and 8 cm in one. The signal intensity of the mural nodules of 11 lesions on T1-weighted images was low in two, intermediate in nine (Figs. 1, 2), and low in one; the signal intensity on T2-weighted images was intermediate in three (Fig. 2), slightly high in three, and low and high mixed in four (Fig. 1). All of the mural nodules were enhanced by contrast material.

The MRI findings of 26 carcinomas in group B morphologically were the solid type in 24 lesions (Figs. 3–5) and the cystic type in 2 lesions (Table 2). The signal intensity of solid components in 24 solid lesions on T1-weighted images was low in one, intermediate in twenty (Figs. 4, 5), intermediate and high mixed in three (Fig. 3); on T2-weighted images and the signal intensity was intermediate in one, heterogeneous intermediate in five, slightly high in four, low and high mixed in three, heterogeneously high in eleven (Figs. 4, 5). Solid components showed various degrees of contrast enhancement by contrast material. All cystic components seen in solid-type lesions exhibiting low signal intensity on T1-weighted images and very high signal intensity on T2-weighted images histologically reflected necrosis or cystic degeneration. MRI showed bilateral ovarian involvement in 1 of 12 patients in group A and in 7 of 19 patients in group B (Fig. 4). MRI detected peritoneal disseminations in one of three patients with stage III disease in group A and in six of eight patients with stage III disease in group B (Fig. 5).

Fig. 3. A 31-year-old woman of pT2cN0M1 (grade 2) without an endometrioma. **A** Sagittal spin-echo T1-weighted MR image (600/12) shows a 10-cm lobular solid mass of heterogeneous mixed iso- and hyperintensity. **B** Sagittal turbo spin-echo T2-weighted MR image (3000/96) shows a solid mass with an ill-defined margin of posterior and inferior portion reflecting capsular rupture (*arrows*) as heterogeneous mixed hypo- and hyperintensity. Ascites is noted. **C** Fat suppression, gadolinium-enhanced sagittal spin-echo T1-weighted MR image (600/12) shows heterogeneous enhancement of the solid mass. **D** Sagittal turbo spin-echo T2-weighted MR image (3000/96) shows diffusely thickened endometrium as isointense, reflecting uterine carcinoma (*arrowheads*)

Discussion

Generally, MRI is useful for the detection and characterization of adnexal masses. Three specific MRI criteria—combination of solid and cystic portions in a lesion, identification of necrosis in a solid lesion, the presence of an irregular wall or thickened septum >3 mm, papillary projections in a cystic lesion—may be employed to differentiate malignant from benign ovarian lesions. The use of gadopentetate dimeglumine facilitates this differentiation and differentiates a malignant mural nodule from a clot or debris.[9,11] In our study, all the cystic-type mural nodules were enhanced by gadopentetate dimeglumine. Of 39 ovarian endometrioid carcinomas in our series, 26 (67%) were predominantly the solid type and 13 (33%) were a large cyst with one or more mural nodules. These findings suggest malignant tumor but are not specific. When it is the cystic type, the MRI findings mimic those of clear cell carcinoma, serous cystadenocarcinoma, adenofibroma, or Mullerian mucinous borderline tumor. When it is the solid type, the MRI findings mimic those of clear cell carcinoma, serous cystadenocarcinoma, metastatic tumor, Mullerian mucinous borderline tumor, or sex cord stromal tumor.

Togashi et al. reported that typically the signal intensity of benign endometriomas is hyperintense on T1-weighted images and hypointense on T2-weighted images due to the magnetic susceptibility effect generated by old hemorrhage or densely concentrated fluid or fibrosis; this "shading" on T2-weighted images was noted in 55 (64%) of 86 benign ovarian endometriomas.[12] These typical finding were not observed in our series. Among 11 cystic-type lesions in group A, the cysts of 5 lesions were hypointense on T1-weighted images and the cysts of 6 lesions were hyperintense on T1- and T2-weighted images without "shading." In regard to this phenomenon, Tanaka et al. reported that the adenocarcinoma cells may produce some fluid or materials that dilute the thick hemorrhagic fluid.[12] Though pathological proof could not be obtained in this clinical review, physicians

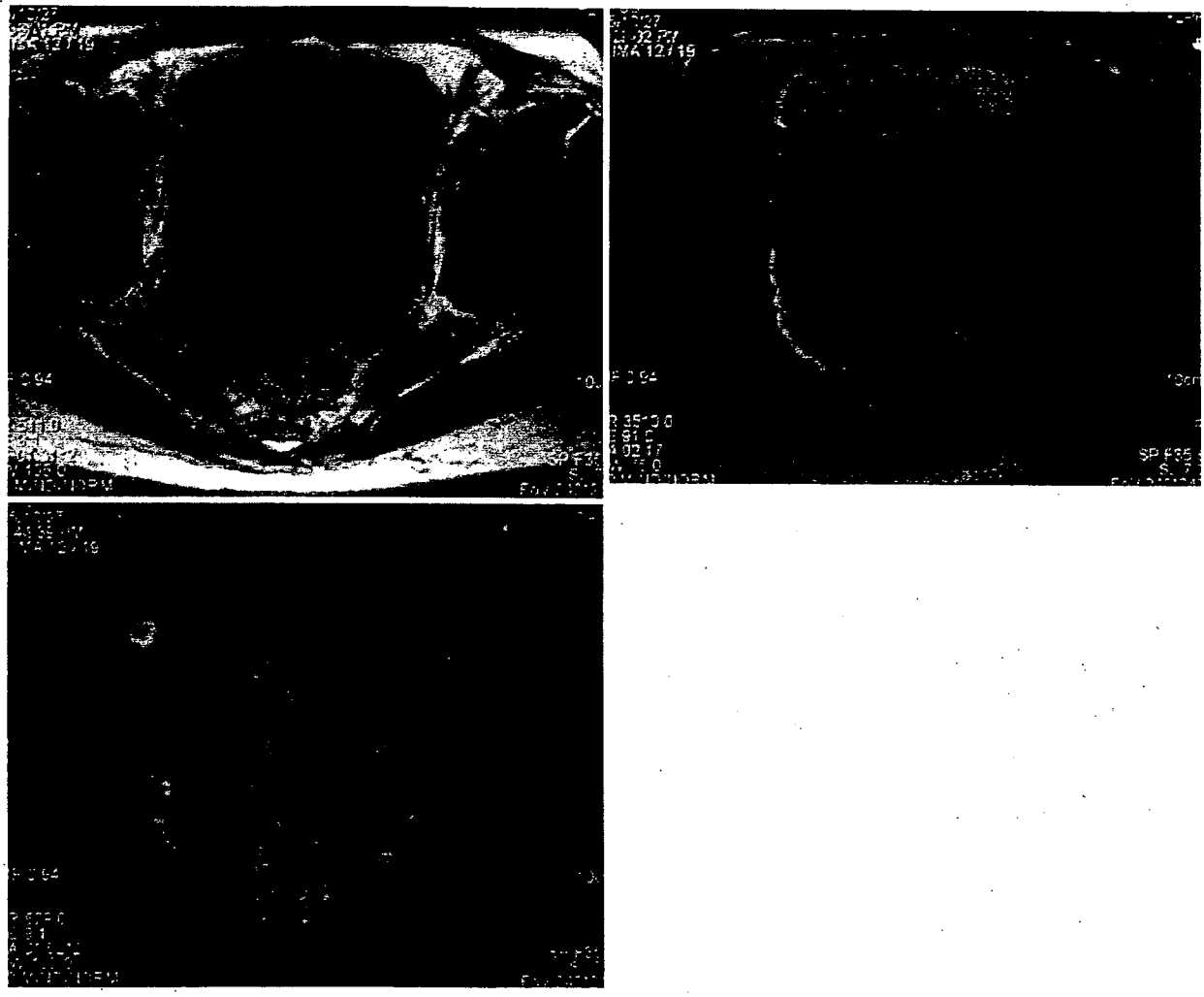

Fig. 4. A 53-year-old woman of pT2cN0M0 (grade 3) without endometrioma. **A** Axial spin-echo T1-weighted MR image (510/9) shows isointense bilateral solid masses (9 cm on the right, 5 cm on the left). **B** Axial turbo spin-echo T2-weighted MR image (3510/91) shows bilateral masses of heterogeneous hyperintensity. Ascites is noted. **C** Fat suppression, gadolinium-enhanced axial spin-echo T1-weighted MR image (600/12) shows the strong enhancement of the bilateral masses invading the uterine serosa

should keep in mind that the preexisting endometrioma in ovarian endometrioid carcinoma rarely shows "shading" on T2-weighed images.[13,14]

Komiyama et al. reported that in a study of 21 ovarian clear cell carcinomas in stage Ic the incidence of positive intraabdominal cytology from some lesions originating from endometrioma was significantly less than that of others without endometrioma.[15] This finding suggests that the coexistence of an endometrial lesion represses hyperplasia or implants of cancer cells. Their hypothesis regarding ovarian clear cell carcinoma may apply to our study of ovarian endometrioid adenocarcinoma. There might be different mechanisms of biological occurrence between groups A and B, even if it is the same endometrioid adenocarcinoma.

Five patients in our study had pathologically confirmed coexisting uterine cancer (16%): four patients were diagnosed as having double cancer, and one patient was suspected of dissemination through the fallopian tube. Only three cases of double cancers (60%) could be detected as thickened endometrium on MRI (Fig. 3). It is difficult to detect small uterine cancers on MRI, but we should carefully observe the uterine endometrium as well as ovarian cancer.

Our study has some limitations because of its retrospective nature, small sample size, use of two different types of MR equipment, and exclusion of patients who had received preoperative chemotherapy. Although dynamic subtraction MRI is useful for depicting small contrast-enhanced nodules in the hyperintense endome-

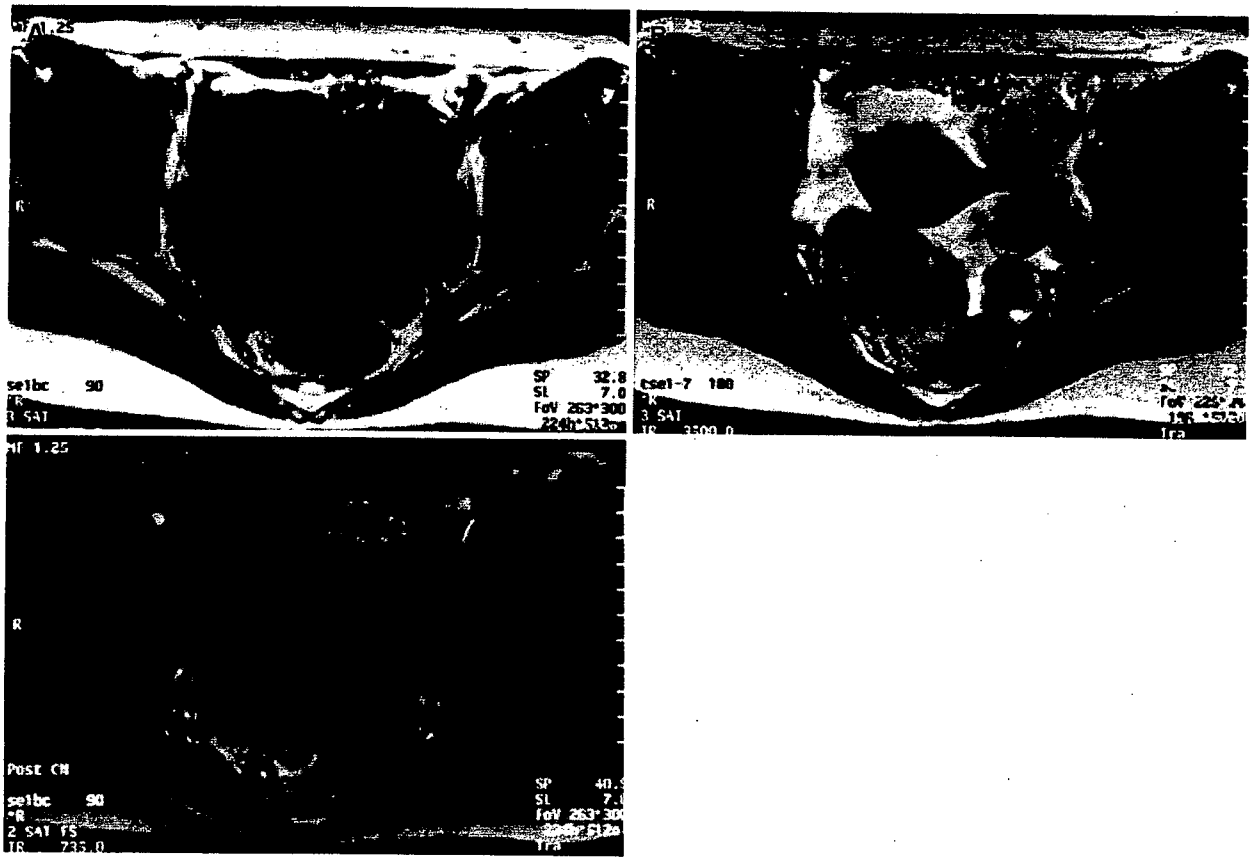

Fig. 5. A 37-year-old woman of pT3cN0M0 (grade 3) without endometrioma. **A** Axial spin-echo T1-weighted MR image (600/12) shows diffuse isointense dissemination along the left uterine round ligament, Douglas pouch, mesenterium, and peritoneum. **B** Axial turbo spin-echo T2-weighted MR image (3500/96) shows diffuse dissemination of slight hyperintensity. Ascites is noted. **C** Fat suppression, gadolinium-enhanced axial spin-echo T1-weighted MR image (600/12) shows heterogeneous enhancement of the intraabdominal dissemination

trioma on T1-weighted images,[11,12] this pulse sequence was not used in our study. In this context, further study should be conducted. Moreover, it is usually difficult to judge pathologically whether a malignant tumor arose from preexisting endometrioma,[1,3,4] and two cases of cystic type pathologically diagnosed as lacking endometriomal tissue in our series may actually arise from endometrioma.

Conclusion

MRI examination of ovarian endometrioid adenocarcinomas revealed two types: a predominantly solid lesion or a large cyst with one or more mural nodules. These findings suggest malignant tumor but are not specific. The lesions arising from endometrioma tended to be of the cystic type on MRI and have a lower nuclear grade and less advanced clinical stage than lesions without endometrioma. Preexisting endometrioma in this entity rarely showed "shading" on T2-weighted images.

Acknowledgments. We thank the gynecologists, especially Yasuihito Takeuti, Kazuaki Katayama, and Takeshi Maruo, for recruiting patients to undergo MRI, as well as the pathologists, especially Kimio Hashimoto and Chiho Obayashi.

References

1. Kline RC, Wharton JT, Atkinson EN, Burke TW, Gershenson DM, Edwards CL. Endometrioid carcinoma of the ovary: retrospective review of 145 cases. Gynecol Oncol 1990;39:337–46.
2. Seidman JD, Russell P. Endometrioid tumors. In: Kurman RJ, editor. Blaustein's pathology of the female genital tract. 5th edition. New York: Springer Verlag; 2002. p. 863–72.
3. Sampson JA. Endometrial carcinoma of the ovary, arising in endometrial tissue in that organ. Arch Surg 1925;10:1–72.
4. Czernobilsky B, Silverman BB, Mikuta JJ. Endometrioid of the ovary. Cancer 1970;26:1141–52.

5. Jimbo H, Yoshikawa H, Onda T, Yasugi T, Sakamoto A, Taketani Y. Prevalence of ovarian endometriosis in epithelial ovarian cancer. Int J Gynecol Obstet 1997;59:245–50.
6. Matsuoka Y, Ohtomo K, Araki T, Kojima K, Yoshikawa W, Fuwa S. MR imaging of clear cell carcinoma of the ovary. Eur Radiol 2001;11:946–51.
7. Fujiwara T, Sugimura K, Yoshizako T, Imaoka I, Kitao M. MR findings of two cases of endometrial carcinoma accompanied with endometrial cyst (in Japanese). Jpn J Clin Radiol 1994;39:983–6.
8. Hayashi T, Kato T, Hasumi K, Yamashita T, Sato M, Kumazaki T. MR imaging of endometrioid carcinoma of the ovary (in Japanese). Jpn J Clin Radiol 2000; 45:1543–8.
9. Hricak H, Chen M, Coakley FV, Kinkel K, Yu KK, Sica G, et al. Complex adnexal masses: detection and characterization with MR imaging—multivariate analysis. Radiology 2000;214: 39–46.
10. Stevens SK, Hricak H, Stern JL. Ovarian lesions: detection and characterization with gadolinium-enhanced MR imaging at 1.5T. Radiology 1991;181:481–8.
11. Outwater EK, Huang AB, Dunton CJ, Talerman A, Capuzzi DM. Papillary projections in ovarian neoplasms: appearance on MRI. J Magn Reson Imaging 1997;7:689–5.
12. Togashi K, Nishimura K, Kimura I, Tsuda Y, Yamashita K, Shibata T, et al. Endometrial cysts : diagnosis with MR imaging. Radiology 1991;180:73–8.
13. Tanaka YO, Yoshizako T, Nishida M, Yamaguchi M, Sugimura K, Itai Y. Ovarian carcinoma in patients with endometriosis: MR imaging findings. AJR Am J Roentgenol 2000; 175:1423–30.
14. Takeuchi M, Matsuzaki K, Uehara H, Nishitani H. Malignant transformation of pelvic endometriosis: MR imaging findings and pathologic correlation. Radiographics 2006;26: 407–17.
15. Komiyama S, Aoki D, Tominaga E, Susumu N, Udagawa Y, Nozawa S. Prognosis of Japanese patients with ovarian clear cell carcinoma associated with pelvic endometriosis; clinicopathologic evaluation. Gynecol Oncol 1999;72:342–6.